PAPER

Density functional theory and experimental studies of caffeic acid adsorption on zinc oxide and titanium dioxide nanoparticles

Tianshi Zhang, Patrick Wojtal, Oleg Rubel and Igor Zhitomirsky*

The outstanding adsorption properties of proteins, containing catecholic amino acid, L-3,4-dihydroxyphenylalanine (DOPA), and recent advances in nanoparticle functionalization using molecules from the catechol family have generated interest in the investigation of catechol adsorption and applications of catecholates in nanotechnology. Caffeic acid (CA) is the closest molecular analogue of DOPA. Density functional theory has been applied for the modelling of CA adsorption on the surface of ZnO and TiO_2. Different adsorption modes have been investigated and corresponding adsorption energies were evaluated. According to the calculated energies, the adsorption of CA is energetically favourable at both surfaces with a stronger affinity to TiO_2. The results of theoretical studies were supported by experimental investigations of CA adsorption. The use of CA as a dispersant for hydrothermal synthesis of ZnO allowed for the fabrication of ZnO nanorods with reduced size and increased aspect ratio. The CA, adsorbed during the hydrothermal synthesis on ZnO nanorods, allowed for their electrosteric dispersion and the electrophoretic deposition (EPD) of ZnO films from stable colloidal suspensions. In another strategy, CA was added as a dispersant for the dispersion of TiO_2 nanorods and the EPD of TiO_2 films. The advantages of catecholates for the synthesis of nanoparticles and fabrication of thin films are discussed.

1. Introduction

The surface modification of materials using molecules of the catechol family is emerging as a new area of technological and scientific interest.[1] Special attention to the adsorption of catecholates on inorganic particles resulted from the fundamental investigations of proteins, containing monomers with catechol ligands, which allowed for strong mussel adhesion to various surfaces.[2–5] It was found that such protein macromolecules contain catecholic amino acid, L-3,4-dihydroxyphenylalanine (DOPA), which interacts strongly with metal atoms on the particle surface.[3] Different adsorption mechanisms were suggested, such as bidentate chelating bonding or bidentate bridging bonding.[2,3] These studies have generated significant interest in the use of DOPA for the synthesis of advanced moisture resistant polymer adhesives.[1,2] The adsorption of catecholates resulted in advanced magnetic, optical, photovoltaic and charge-transfer properties[6] of inorganic nanoparticles. Anionic and cationic molecules of the catechol family attracted significant interest for the fabrication of thin films from stable colloidal suspensions.[6] In this strategy, the catechol ligands of the molecules contribute to their strong adsorption on the

surface of inorganic particles, whereas anionic or cationic groups imparted a charge for efficient electrostatic or electrosteric dispersion.[6,7] Future expansion of this work requires better understanding of the adsorption mechanisms.

The adsorption of catecholates on TiO_2 and ZnO is of particular interest for the development of sensors, photovoltaic and optical devices.[6] Especially promising are applications of catecholates for the dispersion of nanoparticles in colloidal suspensions, synthesis of non-agglomerated nanoparticles of controlled size and deposition of inorganic films by colloidal and electrochemical methods. Caffeic acid (CA) is the closest molecular analogue of DOPA (Fig. 1). Similar to DOPA, the structure of CA contains a catechol ligand. The use of DOPA for colloidal processing of inorganic materials presents difficulties due to zwitterionic properties of this molecule, containing anionic carboxylic group and cationic amino group. In contrast, the structure of CA includes only anionic carboxylic group, which can impart a negative charge for the electrostatic dispersion of particles, containing adsorbed CA.

Ab initio electronic structure calculations, such as the density functional theory (DFT),[8–10] is a popular choice for modelling the adsorption of molecules on inorganic surfaces. DFT is used not only to qualitatively assess the binding affinity and confirmation of molecules at various surfaces, but also to evaluate changes in the optical absorption spectra and vibrational properties of molecules, resulting from their adsorption on the

Department of Materials Science and Engineering, McMaster University, 1280 Main Street West, Hamilton, Ontario, Canada, L8S 4L7. E-mail: zhitom@mcmaster.ca; Tel: +1 (905) 525 9140
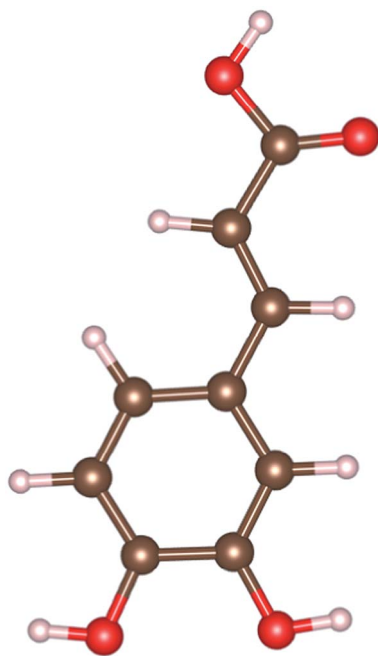
Fig. 1 Chemical structure of CA.

surface. Theoretical calculations combined with various spectroscopic measurements (absorption, photoemission, Raman) become a powerful tool that helps to elucidate details of the adsorption mechanism. Several illustrative examples are listed below.

In the case of chlorogenic acid adsorption on the surface of colloidal silver nanoparticle, the comparison of experimentally observed enhancements and shifts of the Raman bands with DFT calculated vibrational spectra allowed to conclude that their interaction takes place primarily through the oxygen of the carboxylate group.[11] DFT has been successfully used for the analysis of vibrational spectra[12] of adsorbed molecules. Sánchez-de-Armas et al. analyzed the electronic structure and the optical response of catechol, bound to TiO_2 nano clusters, using DFT and time-dependent DFT.[13] It was shown that the absorbance is sensitive to the binding configurations, such as molecular monodentate or bidentate complexes. The bidentate configuration with two catecholate oxygens bonded to one surface Ti atom was the most stable mode. However, the energy difference between the monodentate and bidentate configurations decreased with increasing nanocluster size. Experimental observations of a strong red shift in the TiO_2 absorption threshold, caused by catechol adsorption, was reported by Persson et al.[14] and explained by electronic levels introduced by catechol in the TiO_2 band gap. The authors arrived at this conclusion by comparing experimental adsorption energies with those calculated using a post-Hartree–Fock level theory. The ability to tune the absorption spectrum is particularly important for dye-sensitized solar cells. The theoretical calculations by Li et al.[15] showed that the shape of the adsorption spectrum for catechol adsorbed on $TiO_2(110)$ is sensitive to the orientation of catechol molecules with respect to the surface plane.

The magnitude of the adsorption energy of catechol on TiO_2 evaluated with DFT varies between -0.7 and -2.0 eV per molecule.[16–18] The variation can be attributed to differences in TiO_2 surface structure (anatase or rutile), variety of bonding configurations and flavours of exchange-correlation functionals used in DFT. In spite of the uncertainty in the magnitude of the binging energy, numerous experiments and theoretical studies clearly agree that adsorption of catechol on the surface of TiO_2 is an exothermic process.

The goal of this investigation was the analysis of CA adsorption on rutile TiO_2 and wurtzite ZnO particles by DFT and experimental methods. The results of DFT analysis presented below provide an insight into the mechanism of CA adsorption on TiO_2 and ZnO as well as related adsorption energies. The CA adsorption was confirmed by different experimental methods. The important finding was the possibility of the fabrication of ZnO nanorods with reduced particle size and increased aspect ratio using CA as a dispersant. Moreover, the adsorbed CA allowed for the EPD of ZnO and TiO_2 films from stable suspensions. The results of this investigation pave the way for the application of CA and other catecholates for the synthesis of nanoparticles and deposition of thin films.

2. Methods

2.1. First-principle calculations

The Vesta 3 package[19] was used for three-dimensional visualization of atomic structures. The first-principles calculations were carried out in the framework of the DFT.[20] ABINIT package[21,22] and projector augmented-wave method[23] were used with pseudopotentials adopted from a "GBRV" (version 1.2) library.[24] Perdew et al.[25] version of the generalized gradient approximation (GGA-PBE) was employed for the exchange correlation functional. Completeness of the plane wave basis set was controlled though the cut-off energy, which was set at 15 Ha (408 eV) as determined from convergence studies described below.

The lattice constant of bulk TiO_2 (rutile) and ZnO (wurtzite) were optimized self-consistently by simultaneous minimization of Hellmann–Feynman forces acting on atoms and stresses. The Brillouin zone of the primitive cell was sampled using $6 \times 6 \times 8$ and $8 \times 8 \times 4$ k-mesh for TiO_2 and ZnO, respectively. Calculated lattice parameters are summarized in Table 1 and compared with the literature data.[26,27] The lattice parameters are slightly overestimated (less than 3%), which is a typical trend for calculations of solids with GGA-PBE exchange-correlation

Table 1 Lattice parameters of bulk TiO_2 and ZnO, calculated with DFT in comparison with literature[26,27] experimental data. The fractional coordinate of oxygen (u) in both structures is specified

Compound	Calculated with DFT-PBE			Experimental		
	$a = b$ (Å)	c (Å)	u	$a = b$ (Å)	c (Å)	u
TiO_2 (rutile)	4.646	2.963	0.3047	4.594	2.959	0.3048
ZnO (wurtzite)	3.273	5.333	0.3767	3.250	5.207	0.382

energy functional.[28] The surface of TiO$_2$ was constructed by creating a supercell and truncating it in (110) plane. The choice of non-polar (110) surface is explained by its high thermodynamic stability and abundance in laboratory samples, while other faces tend to reconstruct upon heating at high temperatures and produce (110) facets.[29] Seven monolayers of TiO$_2$ spaced by 17 Å of vacuum in direction perpendicular to the (110) plane were selected to represent the bulk material. The surface structures was then relaxed by minimizing the forces acting on atoms below 1 mHa per Bohr except for two monolayers of atoms in the middle of the slab that remain fixed at their "bulk" positions. Similar strategy was utilized for modelling a ZnO surface. In ZnO both (10$\bar{1}$0) and (11$\bar{2}$0) surfaces are non-polar, stable and exhibit lowest formation energies, which are twice less than the energy of polar surfaces.[30] Micro- and nanocrystals of ZnO typically have hexagonal shape with faces that correspond to (10$\bar{1}$0) family planes.[31] Here we restrict the study to the (10$\bar{1}$0) surface of ZnO. The k-mesh of $1 \times 2 \times 2$ and $1 \times 1 \times 2$ was used for sampling of the supercell Brillouin zone in TiO$_2$ and ZnO supercells, respectively.

The affinity of CA to the surface of TiO$_2$ and ZnO was evaluated by calculation of an adsorption enthalpy H_{ads}, which represents a difference between the total energy E_{tot} of bound and unbound states.

$$H_{ads} = E_{tot}^{bound} - E_{tot}^{unbound} \qquad (1)$$

In modelling of the unbound state, CA (Fig. 1) was placed in the vacuum region between two adjacent surfaces to keep it equidistant (approximately 5 Å) away the surfaces. Atomic positions of the surface structure with the CA in vacuum were optimized *via* minimization of forces once again, while restricting CA from drifting within the cell. Two structures (TiO$_2$ and ZnO) with CA obtained in this manner form a reference "unbound" state, and the corresponding electronic total energy was used in calculation of the adsorption enthalpy (eqn (1)). Convergence studies performed with the increased cutoff energy of 20 Ha indicated that the reported values of the adsorption enthalpy are accurate within ±0.05 eV.

Two different strategies were used to construct a bound state. In the first place, the bound state was formed by desorption of two hydrogens from OH groups bonded to adjacent atoms on the carbon ring, anchoring the CA to the surface, creation of oxygen surface vacancy and formation of water molecule. In the second place, the hydrogen atoms were attached to undercoordinated oxygen atoms at the surface. Obtained structures were allowed to relax, and the corresponding total energy was used in calculations to represent a "bound" state. It should be noted that the number of atoms is conserved in the course of this transformation and total energies can be directly used to evaluate the adsorption enthalpy using eqn (1).

2.2. Materials and experimental methods

Caffeic acid (CA), TiO$_2$ (rutile) nanorods and zinc acetate dihydrate (Aldrich) were used as starting materials. According to the manufacturer, the TiO$_2$ nanorods had a typical diameter of 10

nm and length of 40 nm. For the synthesis of ZnO nanorods, 10 mL of 0.1 M of zinc acetate solution in ethanol was mixed with 20 mL solution of 0.5 M NaOH in ethanol, containing 0.003 M CA or without CA. The mixed solution was transferred to a Teflon-lined stainless steel autoclave and heated at 150 °C for 24 hours. Electrophoretic deposition was performed from 4 g L^{-1} TiO$_2$ and ZnO suspensions in ethanol at deposition voltages of 30–50 V. The electrochemical cell for electrophoretic deposition (EPD) contained a 304 type stainless steel substrate and a Pt counterelectrode with dimensions of $30 \times 50 \times 0.1$ mm. The distance between the electrodes was 15 mm.

X-ray diffraction (XRD) investigations were performed using a powder diffractometer (Nicolet I2, monochromatized CuK$_\alpha$ radiation) at a scanning speed of 0.5° min^{-1}. Electron microscopy studies were performed using a transmission electron microscope (JEOL JEM 1200 EX TEMSCAN) and a scanning electron microscope (SEM, JOEL JSM-7000F). The films, deposited by EPD were removed from the substrates and collected materials were used for Fourier transform infrared spectroscopy (FTIR). FTIR studies were performed on Bio-Rad FTS-40 instrument.

3. Results and discussion

Here we restrict the study to adsorption of CA molecule on non-polar surfaces. Non-polar surfaces in polar solids are characterized by an equal number of cation and anion dangling bonds that result in a self-compensation of the surface states. Thus an insulating electronic structure is preserved at the surface without defect states present within the band gap. High thermodynamic stability of non-polar surfaces is indicative of their resistance to structural changes that can perturb the cation–anion dangling bond balance and lead to unfavourable high-energy defect states. Favourable adsorption of molecules at the surface is possible, provided the newly formed structure conserves the bond order, *i.e.*, does not introduce an excess number of cation (or anion) dangling bonds. This restriction constitutes a fundamental difference between adsorption of molecules at metallic and insulating surfaces.

TiO$_2$ (110) non-polar surface consists of alternating rows of 2-fold coordinated oxygen bridges and tranches with 5-fold coordinated Ti-atoms at the bottom (Fig. 2). This arrangement is different from the bulk, where Ti and O exhibit 6-fold and 3-fold coordination, respectively. Undercoordinated Ti-atoms at the surface donate their electrons (2/3e per dangling bond) to the oxygen bridges that are capable of accepting exactly 2/3e each (Fig. 3(a)). Undercoordinated Ti-atoms are obvious candidates for anchoring the CA molecules (Fig. 2(a and b)). This newly formed structure seems to be plausible as the number of undercoordinated Ti atoms at the surface is reduced. However, it will simultaneously lead to undersaturation of O-bridges and formation of defect (acceptor) states. One possibility to restore the charge balance is by creating an oxygen vacancy (V$_O$) at the surface (Fig. 3(b)). Oxygen desorbed from the surface reacts with two hydrogens cleaved from CA by forming a water molecule. The reaction proceeds as follows:
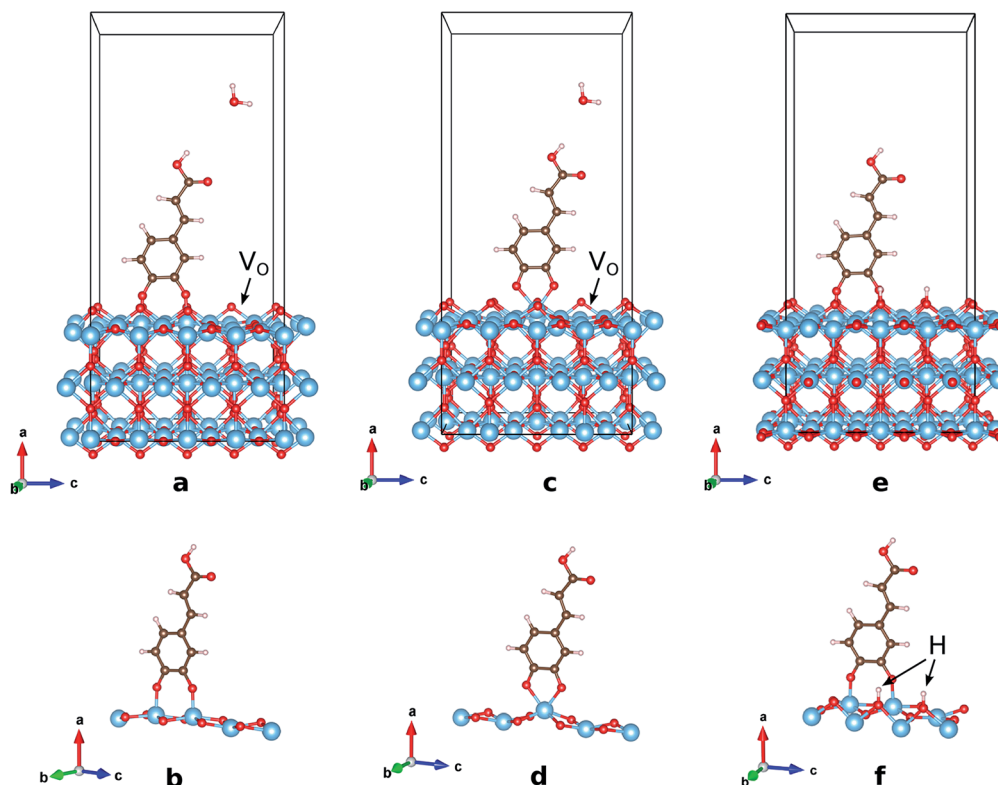
Fig. 2 Adsorption of CA at the (110) surface of TiO_2 (rutile) in two alternative bonding configurations: (a and b) bridging bidentate and (c–f) chelating bidentate. The adsorption can be accompanied by formation of the surface oxygen vacancy (V_O) and the water molecule as shown on panels (a and c). Alternatively, the pair of hydrogen atoms cleaved from the CA are accommodated at the oxygen bridges (e and f).

$$TiO_2 + C_9H_8O_4 \rightarrow TiO_2(V_O) + C_9H_6O_4 + H_2O. \qquad (2)$$
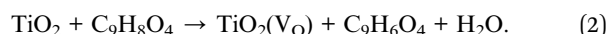
DFT study of two alternative adsorption configurations (Fig. 2(b and d)) reveals that both bridging bidentate and chelating bidentate arrangements result in a favourable adsorption enthalpy of −1.3 and −0.6 eV, respectively. The bridging bidentate structure is energetically more favourable as evident from the two times larger magnitude of the adsorption enthalpy. This result can be explained by overcoordination (7-fold) of Ti atom in the case of chelating bidentate structural

model, while the new Ti–O bonds in the bridging bidentate bonding model naturally resemble the bulk TiO_2.

Another possibility to restore the charge balance on TiO_2 surface with CA is to form OH-bond between the cleaved hydrogen atoms and the two-fold coordinated oxygen atoms (Fig. 2(f)). The resultant structure does not require additional defects for the charge compensation (Fig. 3(c)) and thus has the lowest formation enthalpy of −2.65 eV.

Similar strategy was employed for the analysis of CA adsorption on the non-polar ($10\bar{1}0$) surface of ZnO. Three alternative bonding configurations were considered: the modified chelating bidentate, bridging bidentate with an oxygen
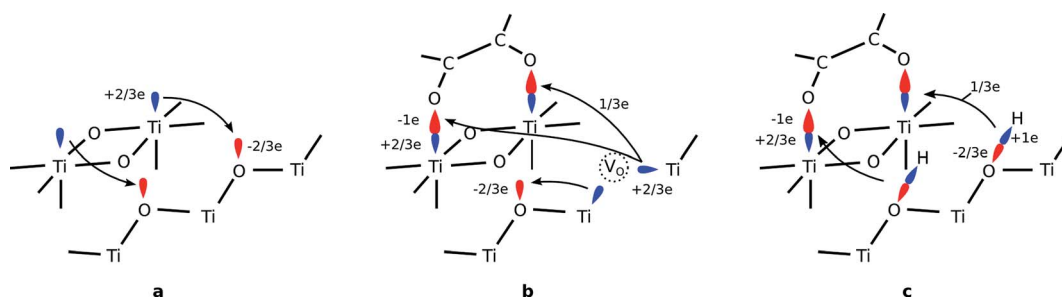

Fig. 3 Self compensation of dangling bonds at the non-polar (110) surface of (a) TiO_2 and (b and c) TiO_2 with CA adsorbed in a bridging bidentate configuration. Two possible strategies for saturation of excess acceptor states introduced by CA are considered: (b) formation of an oxygen vacancy V_O or (c) accommodation of a pair of hydrogen atoms at the oxygen bridges.

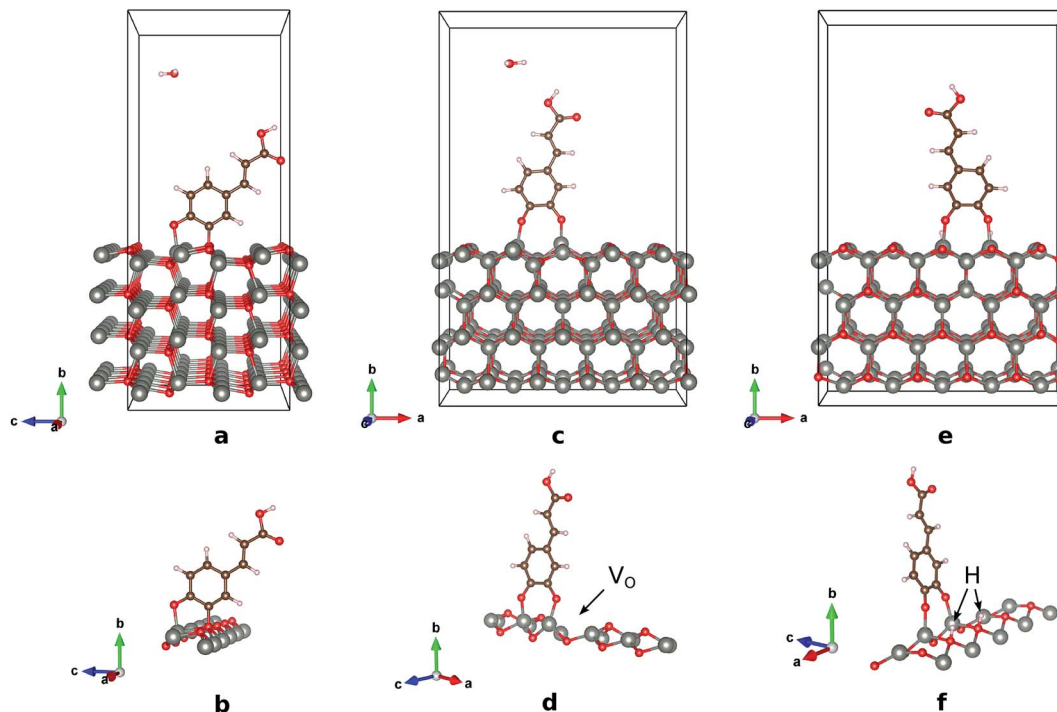**Fig. 4** Adsorption of CA at the (10$\bar{1}$0) surface of ZnO in two alternative bonding configurations: (a and b) modified chelating bidentate and (c–f) bridging bidentate. The bridging bidentate adsorption configuration requires compensation of bond charges, which can be accomplished either (d) by formation of the surface oxygen vacancy (V_O) shown by the arrow or (c) by establishing two O–H bonds with under-coordinated oxygen atoms at the surface.

vacancy and without it (Fig. 4). DFT results suggest that the modified chelating bidentate structure shows a favourable adsorption with the enthalpy of −0.45 eV. In this structure, CA adsorption restores 4-fold coordinations of Zn and O atoms at the surface and no vacancy formation is required (Fig. 5). A positive adsorption enthalpy of +0.65 eV for the bridging bidentate configuration can be attributed to large distortions at the surface caused by the vacancy (see Fig. 4(d)). The bridging bidentate configuration without a defect (Fig. 4(f)) exhibits the strongest adsorption enthalpy of −1.50 eV. It should be noted that in spite of the efforts to enforce the charge neutrality at the surface of ZnO with CA, the electronic structure calculations reveal the presence of defect states with fractional occupancy at the Fermi energy. The presence of defect states can explain

a relatively weak interaction energy between CA and ZnO surface, as compared to the TiO$_2$ surface.

DFT with local exchange correlation functionals, such as GGA, describes well a vast number of compounds. However, titanium and zinc belong to transition metals with strong electronic correlations due to localized d-orbital that cannot be accurately captured by GGA alone. This shortcoming is remedied by introducing a mean-field-like Hubbard screened coulomb interaction between correlated electrons U, the so-called DFT+U approach.[32] Here we select $U = 2$ and 8 eV for TiO$_2$ and ZnO, respectively, based on the prior DFT studies.[33,34] The adsorption enthalpy was re-evaluated for the configurations with the strongest binding affinity of CA to the surface taking into account correlation effects. In the case of TiO$_2$, the
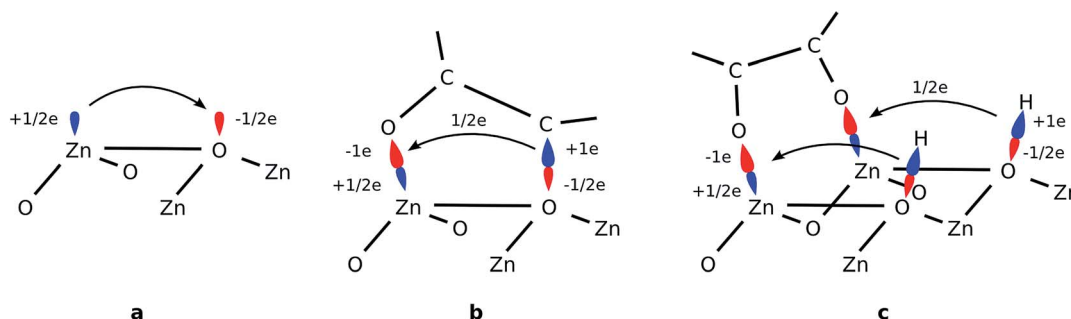

Fig. 5 Self-compensation of dangling bonds at the non-polar (10$\bar{1}$0) surface of (a) ZnO, (b) ZnO with CA adsorbed in a modified chelating bidentate configuration and (c) ZnO with CA adsorbed in a bridging bidentate configuration.
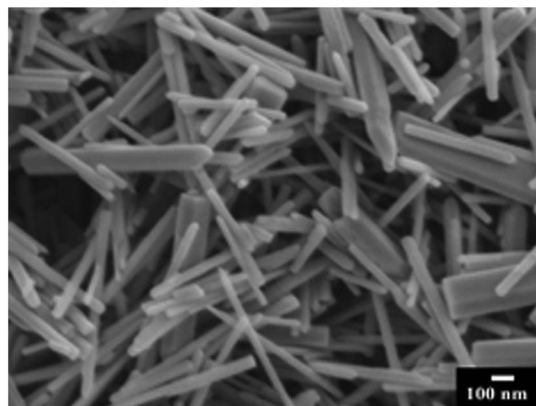
Fig. 6 SEM image of ZnO nanorods, prepared by the hydrothermal synthesis method.

Fig. 8 X-ray diffraction pattern of ZnO prepared (A) without and (B) in the presence of CA (▼ – peaks, corresponding to the JCPDS file 36-1451).

adsorption enthalpy of -2.64 eV is obtained with DFT+U, which is not different from the value of -2.65 eV reported above. The strongest adsorption enthalpy on ZnO surface calculated with DFT+U amounts to -1.61 eV that is close to -1.50 eV obtained without the correction for additional correlation effects. The greater influence of DFT+U on ZnO can be attributed to the stronger U value as compared to TiO$_2$, however the bare DFT-GGA enthalpies remain accurate within 10%.

The adsorption of CA on ZnO and TiO$_2$ was studied by experimental methods. Fig. 6 shows SEM image of rod-like particles, which were prepared by the hydrothermal method. The TEM images of the particles are shown in Fig. 7(A). The electron microscopy data indicated that the typical diameter of the rod-like particles was in the range of 50–250 nm and the length was 0.2–1.5 μm. The size of the ZnO particles prepared in the presence of CA was significantly smaller. The TEM data presented in Fig. 7(A and B) allowed for the comparison of the morphologies of the particles prepared without CA and in the presence of CA. The particles, prepared in the presence of CA showed a nanorod morphology with typical diameter of the nanorods in the range of 10–30 nm and length of 0.2–1 μm. The TEM images indicate that the particles, prepared in the presence of CA have higher aspect ratio, compared to the particles, prepared without CA. The X-ray diffraction patterns (Fig. 8) of the particles showed peaks of the wurtzite phase. The 2θ
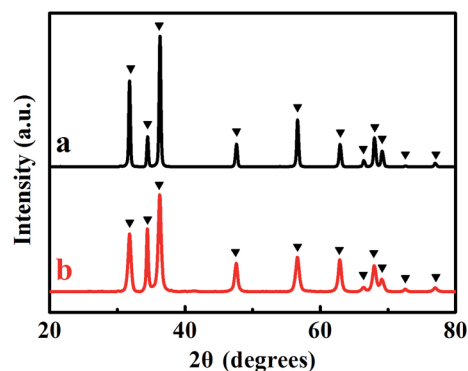
diffraction angles of the peaks in the diffraction pattern are in agreement with the JCPDS file 36-1451. The difference in the relative intensities of the peaks, compared to the JCPDS file 36-1451, can be attributed to the rod-like morphology of the particles.[35] It is suggested that the reduction in the diameter of the ZnO particles, prepared in the presence of CA is related to CA adsorption on the surface of growing ZnO particles during the hydrothermal synthesis. The adsorption of CA on the $(10\bar{1}0)$ plane can inhibit the growth of the ZnO particles. As a result, the diameter of the particles, prepared in the presence of CA, reduced significantly, compared to the diameter of the particles, prepared without CA.

The EPD experiments provided additional evidence of the CA adsorption on the ZnO particles. The ZnO suspensions, prepared without CA were unstable and showed rapid sedimentation immediately after the ultrasonic agitation. In contrast, the suspensions, prepared in the presence of CA, showed good stability for more than one week. EPD has not been achieved from the suspensions of ZnO, prepared without CA. In contrast, ZnO particles, prepared in the presence of CA, were deposited on anodic substrates by EPD. Fig. 9 shows SEM images of ZnO films, deposited by EPD. The films contained ZnO nanorods, the dimensions of the nanorods are in agreement with the TEM data (Fig. 7(B)). The increase in the deposition voltage resulted in increased porosity of the films (Fig. 9(A and B)). The increased porosity can result from gas evolution at the electrode surface. It is suggested that adsorbed CA imparted
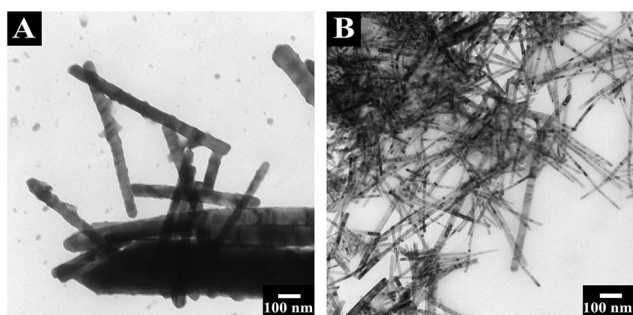

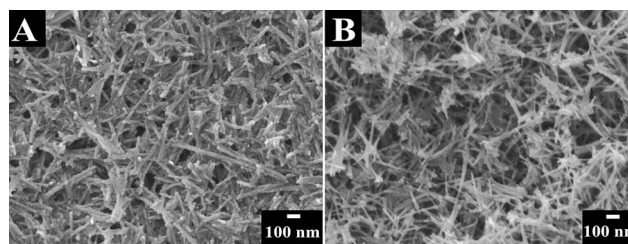**Fig. 7** TEM images of ZnO prepared (A) without CA and (B) in the presence of CA.

Fig. 9 SEM images of the films prepared by EPD at deposition voltages of (A) 30 and (B) 50 V from 4 g L^{-1} suspensions of ZnO, prepared in the presence of CA.

a charge to the ZnO particles and allowed for improved suspension stability and film formation by EPD.

The adsorption of CA on the ZnO nanorods has also been confirmed by the results of FTIR studies of the deposited material (Fig. 10(A)). The absorptions at 1440 and 1650 cm^{-1} are related to symmetric COO^- stretching vibrations and C–C stretching vibrations of aromatic ring of CA,[36,37] respectively. The broad absorption at 3410 cm^{-1} is associated with the stretching vibration of OH groups of adsorbed water molecules.[38]

The adsorption of CA on TiO_2 was confirmed by EPD experiments. The suspensions of TiO_2 nanorods were unstable and showed rapid sedimentation immediately after the ultrasonic agitation. The addition of CA to the suspensions allowed for the fabrication of stable suspensions and EPD of TiO_2 films was achieved from such suspensions. Fig. 11 shows deposit mass *versus* CA concentration in the suspensions. The deposit mass increased with increasing CA concentration and showed a maximum at 0.5 g L^{-1}. The increase in the deposition yield with increasing CA concentration below the maximum can result from increased adsorption of CA on the TiO_2 particles, which allowed for improved suspensions stability and increased particle charge. The decrease in the deposition yield with increasing CA concentration above the maxima can result from increased ionic strength of the suspensions, which was detrimental for the dispersion. The increase in the ionic strength in the suspension resulted in increased current and enhanced gas evolution at the electrode, which led to reduced deposition rate.
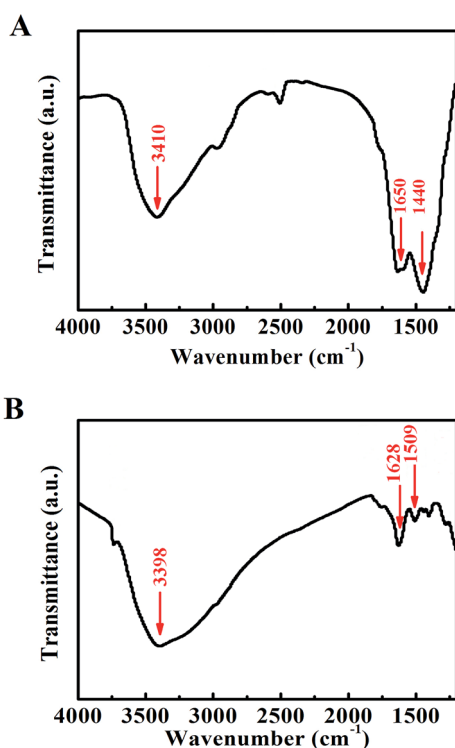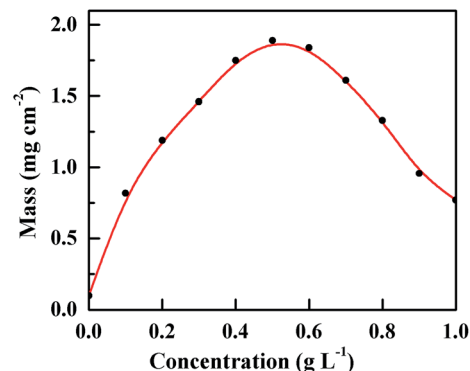

Fig. 11 Deposit mass *versus* CA concentration in the 4 g L^{-1} TiO_2 suspension at a deposition voltage of 100 V and deposition time of 3 min.

The deposition yield in the EPD process depends on many factors, discussed in the literature, such as electric field, electric current, particle concentration, solvent, concentration of dispersant and deposition time.[39,40] The maximum in the Fig. 11 corresponds to optimal CA concentration for the selected deposition conditions. Fig. 12 shows a typical SEM image of the deposited film, containing the TiO_2 nanorods. The size of the nanorods is in agreement with the data, provided by the powder manufacturer. The FTIR analysis of the deposited material (Fig. 10(B)) confirmed the CA adsorption on TiO_2. The absorptions at 1628 and 1509 cm^{-1} can be attributed to C–C stretching vibrations of adsorbed CA.[37] The broad peak at 3398 cm^{-1} can result from stretching vibration of OH groups of adsorbed water molecules.[38]

The experimental results presented above show different avenues for the applications of CA adsorption in materials processing. The adsorption of CA on ZnO during hydrothermal synthesis allowed for the reduction of ZnO particle size and increased aspect ratio of the particles. The particles contained adsorbed CA after synthesis. Such particles were successfully used for the film formation by EPD. It is important to note that CA has a relatively small size, compared to long chain

Fig. 10 FTIR spectra of (A) deposit, obtained by EPD from 4 g L^{-1} suspensions of ZnO, prepared in the presence of CA, (B) deposit, obtained by EPD from 4 g L^{-1} TiO_2 suspension, containing 1 g L^{-1} CA.
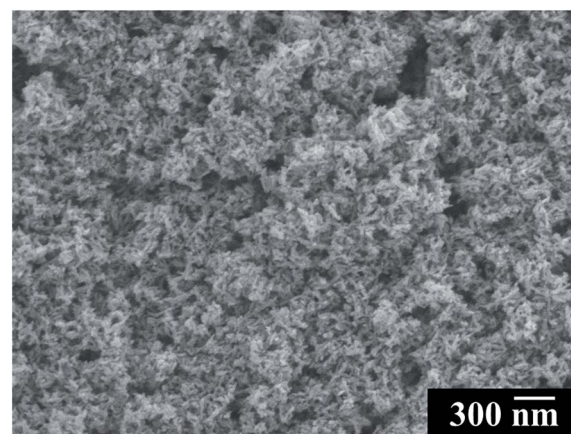

Fig. 12 SEM image of TiO_2 film, prepared from the 4 g L^{-1} TiO_2 suspension at a deposition voltage of 100 V and deposition time of 3 min.

surfactants used for the synthesis of nanoparticles.[41,42] However, long chain surfactants create insulating layers at the particle surface. Such surfactants are usually replaced with smaller surfactants for the particle application in thin film electronic devices.[41,42] The application of long chain surfactants, such as oleic acid, for the synthesis of nanoparticles offers the advantage of improved steric stabilization. The adsorption of oleic acid involves interaction of COO^- group of the acid with metal atoms on the particle surface. However, the adsorption of catechol ligand on the particle surface is superior, compared to that of the carboxyl group.[6] The adsorption of dispersants on the particle surface is critical for the dispersion. A non-adsorbed ionic dispersant acts as an electrolyte, which according to the DLVO theory decreases the suspension stability.[43] Moreover, long chain surfactants can form micelles, which promote depletion-induced aggregation of particles.[44] The catechol ligands of CA allowed for efficient adsorption of CA on the particle surface, whereas COO^- groups provided a charge for electrosteric dispersion. It is suggested that problems with ligand exchange in the development of devices, based on colloidal nanoparticles, can be avoided using anionic and cationic catecholates as efficient dispersants. Another strategy for application of CA is based on the use of this molecule as a charged dispersant for EPD. In our investigation we used commercially available TiO_2 nanorods with relatively small particle size. The addition of CA to the TiO_2 suspensions allowed for particle dispersion and film formation by EPD. The results of this investigation indicated that catecholates are promising dispersants for the synthesis of nanoparticles and film formation by colloidal methods.

4. Conclusions

To deepen the understanding of catecholates adsorption on inorganic surfaces, we have investigated the CA adsorption on ZnO and TiO_2 using DFT. The largest magnitudes of the adsorption enthalpy −2.65 and −1.50 eV for TiO_2 and ZnO, respectively, were obtained for the bridging bidentate bond configuration of CA at the surface that causes least structural changes. Special care was taken to ensure that the proposed bond configurations are compatible with the charge compensation that takes place at stable non-polar surfaces. DFT calculations indicate that the most efficient strategy for the charge compensation is accommodation of a pair of hydrogen atoms cleaved from CA by undercoordinated oxygen atoms at the surface. The adsorption of CA on ZnO and TiO_2 was confirmed by sedimentation tests, EPD experiments, electron microscopy and FTIR data. The use of CA as a dispersant for the hydrothermal synthesis of ZnO allowed for the reduced size and increased aspect ratio of the ZnO nanorods. As-prepared ZnO nanorods, containing adsorbed CA formed stable suspension due to electrosteric dispersing effect of CA. The use of CA as a dispersant allowed for the fabrication of ZnO films. In another strategy, CA was added to the commercial TiO_2 powders and allowed for particle dispersion and EPD. The dispersants from the catechol family offer advantages for colloidal nanotechnology of oxide films due to strong adsorption of the catechol ligands. Future expansion of this work will result

in the development of advanced dispersants for synthesis of nanoparticles and film formation by EPD.

References

1 J. Sedó, J. Saiz-Poseu, F. Busqué and D. Ruiz-Molina, *Adv. Mater.*, 2013, **25**, 653–701.
2 B. P. Lee, P. B. Messersmith, J. N. Israelachvili and J. H. Waite, *Annu. Rev. Mater. Res.*, 2011, **41**, 99–132.
3 H. Lee, S. M. Dellatore, W. M. Miller and P. B. Messersmith, *Science*, 2007, **318**, 426–430.
4 J. H. Waite, *Nat. Mater.*, 2008, 7, 8–9.
5 M. A. Matin, R. K. Chitumalla, M. Lim, X. Gao and J. Jang, *J. Phys. Chem. B*, 2015, **119**, 5496–5504.
6 M. S. Ata, Y. Liu and I. Zhitomirsky, *RSC Adv.*, 2014, **4**, 22716–22732.
7 Y. Liu, M. Ata, K. Shi, G.-z. Zhu, G. Botton and I. Zhitomirsky, *RSC Adv.*, 2014, **4**, 29652–29659.
8 A. Vittadini, A. Selloni, F. Rotzinger and M. Grätzel, *J. Phys. Chem. B*, 2000, **104**, 1300–1306.
9 A. G. Thomas and K. L. Syres, *Chem. Soc. Rev.*, 2012, **41**, 4207–4217.
10 A. Calzolari, A. Ruini and A. Catellani, *J. Am. Chem. Soc.*, 2011, **133**, 5893–5899.
11 N. Biswas, S. Kapoor, H. S. Mahal and T. Mukherjee, *Chem. Phys. Lett.*, 2007, **444**, 338–345.
12 W. J. Barreto, R. A. Ando, B. M. Estevão and K. P. da Silva Zanoni, *Spectrochim. Acta, Part A*, 2012, **92**, 16–20.
13 R. Sánchez-de-Armas, M. San-Miguel, J. Oviedo, A. Marquez and J. Sanz, *Phys. Chem. Chem. Phys.*, 2011, **13**, 1506–1514.
14 P. Persson, R. Bergström and S. Lunell, *J. Phys. Chem. B*, 2000, **104**, 10348–10351.
15 S.-C. Li, J.-g. Wang, P. Jacobson, X.-Q. Gong, A. Selloni and U. Diebold, *J. Am. Chem. Soc.*, 2009, **131**, 980–984.
16 N. Martsinovich, D. R. Jones and A. Troisi, *J. Phys. Chem. C*, 2010, **114**, 22659–22670.
17 P. Redfern, P. Zapol, L. Curtiss, T. Rajh and M. Thurnauer, *J. Phys. Chem. B*, 2003, **107**, 11419–11427.
18 Y. Xu, W.-K. Chen, S.-H. Liu, M.-J. Cao and J.-Q. Li, *Chem. Phys.*, 2007, **331**, 275–282.
19 K. Momma and F. Izumi, *J. Appl. Crystallogr.*, 2011, **44**, 1272–1276.
20 W. Kohn and L. J. Sham, *Phys. Rev.*, 1965, **140**, A1133.
21 X. Gonze, J.-M. Beuken, R. Caracas, F. Detraux, M. Fuchs, G.-M. Rignanese, L. Sindic, M. Verstraete, G. Zerah and F. Jollet, *Comput. Mater. Sci.*, 2002, **25**, 478–492.
22 X. Gonze, *J. Crystallogr.*, 2005, **220**, 558–562.
23 M. Torrent, F. Jollet, F. Bottin, G. Zérah and X. Gonze, *Comput. Mater. Sci.*, 2008, **42**, 337–351.

24 K. F. Garrity, J. W. Bennett, K. M. Rabe and D. Vanderbilt, *Comput. Mater. Sci.*, 2014, **81**, 446–452.

25 J. P. Perdew, K. Burke and M. Ernzerhof, *Phys. Rev. Lett.*, 1996, **77**, 3865.

26 S. Abrahams and J. Bernstein, *J. Chem. Phys.*, 1971, **55**, 3206–3211.

27 H. H. Landolt and R. Börnstein, *New Data and Updates for several Semiconductors with Chalcopyrite Structure, for several II-VI Compounds and diluted magnetic IV-VI Compounds, Landolt-Börnstein - Group III Condensed Matter Series*, Springer, 2013.

28 P. Haas, F. Tran and P. Blaha, *Phys. Rev. B: Condens. Matter Mater. Phys.*, 2009, **79**, 085104.

29 A. L. Linsebigler, G. Lu and J. T. Yates Jr, *Chem. Rev.*, 1995, **95**, 735–758.

30 B. Meyer and D. Marx, *Phys. Rev. B: Condens. Matter Mater. Phys.*, 2003, **67**, 035403.

31 J.-M. Li, X.-L. Zeng, Q. Huang and Z.-A. Xu, *CrystEngComm*, 2012, **14**, 7800–7806.

32 V. I. Anisimov, J. Zaanen and O. K. Andersen, *Phys. Rev. B: Condens. Matter Mater. Phys.*, 1991, **44**, 943.

33 Z. Hu and H. Metiu, *J. Phys. Chem. C*, 2011, **115**, 5841–5845.

34 P. Erhart, K. Albe and A. Klein, *Phys. Rev. B: Condens. Matter Mater. Phys.*, 2006, **73**, 205203.

35 Q. Li, V. Kumar, Y. Li, H. Zhang, T. J. Marks and R. P. Chang, *Chem. Mater.*, 2005, **17**, 1001–1006.

36 M. Cheong and I. Zhitomirsky, *Colloids Surf.*, 2008, **328**, 73–78.

37 I. A. Jankovic, Z. V. Saponjic, M. I. Comor and J. M. Nedeljkovic, *J. Phys. Chem. C*, 2009, **113**, 12645–12652.

38 Y. Wang and I. Zhitomirsky, *Langmuir*, 2009, **25**, 9684–9689.

39 O. O. van der Biest and L. J. Vandeperre, *Annu. Rev. Mater. Sci.*, 1999, **29**, 327–352.

40 E. A. Olevsky, X. Wang, A. Maximenko and M. A. Meyers, *J. Am. Ceram. Soc.*, 2007, **90**, 3047–3056.

41 K. M. Kim, J. H. Jeon, Y. Y. Kim, H. K. Lee, O. O. Park and D. H. Wang, *Org. Electron.*, 2015, **25**, 44–49.

42 S. Ghosh, M. Saha and S. K. De, *Nanoscale*, 2014, **6**, 7039–7051.

43 I. Zhitomirsky, *Adv. Colloid Interface Sci.*, 2002, **97**, 277–315.

44 B. Vigolo, A. Penicaud, C. Coulon, C. Sauder, R. Pailler, C. Journet, P. Bernier and P. Poulin, *Science*, 2000, **290**, 1331–1334.